

Open Charm as a Probe of Pre-Equilibrium Dynamics in Nuclear Collisions ?

Ziwei Lin and Miklos Gyulassy

Department of Physics, Columbia University, New York, NY, 10027

December 15, 1994

Abstract

The pre-equilibrium contribution to open charm production in nuclear collisions at $\sqrt{s} = 200$ AGeV is calculated using three different models for the correlations between momentum and space-time coordinates. Ideal (Bjorken) correlation between the rapidity y and space-time rapidity η of mini-jet gluons suppresses greatly the pre-equilibrium yield and even allowing for the minimal uncertainty correlations leads, in contrast to previous estimates, only to a small pre-equilibrium charm yield as compared to initial yield due to gluon fusion. The “intrinsic” charm process is negligible in the mid-rapidity domain.

I. INTRODUCTION

Open charm production, direct photon, and dilepton production are among the most direct probes [1–4] of the early time evolution of the quark-gluon plasma produced in ultra-relativistic nuclear reactions. At collider energies $\sqrt{s} > 200$ AGeV the initial mini-jet plasma is mostly gluonic [5,6] with a quark content far below its chemical equilibrium value. Furthermore, the initial transverse momentum distribution of those gluons is very broad [2] resembling a hot thermal gas of gluons with an effective temperature $T \sim 500$ MeV [5]. Because charm is produced mainly through gluon fusion, open charm production provides a probe of that initial gluonic state. In contrast, hidden charm [7] is mostly sensitive to final state interactions in the later stages of evolution. Photons and dileptons are complementary probes of the evolution of the suppressed quark component of the plasma.

The present study is motivated by two recent studies [2,4] of open charm which predicted widely different rates in nuclear collisions. In ref. [2] the pre-equilibrium contribution was found to be almost equal to initial gluon fusion rate. A similar factor of 2 enhancement of charm from thermal production in hot-gluon scenario was also suggested [5]. In ref. [4], a more provocative claim was made that open charm may even be enhanced by over an order of magnitude above the initial pQCD rate. The main result of our present study is that correlations between the rapidity y and the space-time rapidity η lead to a large suppression (about a factor of 40) relative to the uncorrelated case. Thus, the pre-equilibrium open charm production is found to be unfortunately a very small fraction of the initial fusion rate. The large enhancement of charm production in ref. [4] is found to be due to an overestimation of the contribution from the flavor excitation processes and the use of a low energy A^α scaling from pp reactions measured at $E_{lab} = 300 - 400$ GeV.

The paper is organized as follows: In section II the dependence of the direct pQCD rates for charm production on structure functions, Q^2 scale, and K factor is reviewed and compared to existing data. The beam energy dependence and the A dependence of the initial charm production are compared to results in ref. [4]. In section III, the pre-equilibrium

charm production is calculated. The mini-jet rapidity and transverse momentum distribution are fit to results of the Monte Carlo HIJING model [8] including initial and final state radiation. Three different models for the space-time and momentum correlations are studied and the influence on the charm yield is calculated. Of the three models, we concentrate on a minimally correlated model resulting from uncertainty principle, which is similar to the type of correlation assumed in ref. [9]. We also study the sensitivity of the results to different models of the formation physics [10]. Section IV contains the summary.

II. INITIAL CHARM PRODUCTION

Heavy quark production in pp reactions was calculated long ago in ref. [11] including both fusion and heavy flavor excitation processes in the leading order pQCD. It was proposed that the flavor excitation processes were dominant at high energies because a small Q^2 exchange can easily liberate any charm component in the nucleon while gluon fusion was suppressed because $Q^2 \geq 4M_c^2$. In the Parton Cascade Model [4], both mechanisms are incorporated to calculate s, c, b quark production in nuclear collisions. There the results suggested that the flavor excitation of the charm quark of nuclear structure functions would be the dominant source of charm production in nuclear collisions as well. However, it is pointed out [12] that the original flavor excitation rates in ref. [11] were too high in the $x_f \sim 0$ region due to neglected interference with other pQCD amplitudes to the same order. When all diagrams were added together, a large destructive interference was found to suppress the flavor excitation rates by powers of Λ/M_q , where $\Lambda \sim 300MeV$ is a typical QCD scale and M_q is the heavy quark mass. The suppression factor appears to the process $g+c(\bar{c})$ where the charm is evolved from the structure functions using *perturbative* QCD, as also shown in ref. [13]. We note that there is a possible non-perturbative charm component (intrinsic charm) in the nucleon. There are experimental constraints on the amount of that non-perturbative charm component [14,15]. The total contribution of the intrinsic charm was shown in refs. [16,17] to be small (about 10%) in the midrapidity region where most of the charm is made.

Although the contribution of the intrinsic charm component appears important at large x_f , its contribution to the total cross section is small and well within the uncertainties from other sources.

In this paper we only include fusion processes for the parton level cross sections as in ref. [2]. For the production in $p - p$ collisions, we use the light quark and gluon structure functions from Glück et al. [18] and Duke-Owens [19] for comparison. The pQCD differential cross sections for $a + b \rightarrow c\bar{c} + X$, are taken from ref. [11]. For example,

$$\sigma_{q\bar{q} \rightarrow c\bar{c}} = \frac{8\pi\alpha_s^2(Q^2)}{27\hat{s}^2}(\hat{s} + 2M_c^2) \chi \quad (1)$$

$$\sigma_{gg \rightarrow c\bar{c}} = \frac{\pi\alpha_s^2(Q^2)}{3\hat{s}} \left[-\left(7 + \frac{31M_c^2}{\hat{s}}\right)\frac{1}{4}\chi + \left(1 + \frac{4M_c^2}{\hat{s}} + \frac{M_c^4}{\hat{s}^2}\right) \log \frac{1+\chi}{1-\chi} \right] \quad (2)$$

where $\chi = \sqrt{1 - 4M_c^2/\hat{s}}$ and we consider the following two choices for the scale Q^2 in the coupling constant $\alpha_s(Q^2) = 12\pi / [(33 - 2n_f) \log(Q^2/\Lambda^2)]$ from ref. [11]:

1. for $gg \rightarrow c\bar{c}$, $Q^2 = \hat{s}/2$; for $q\bar{q} \rightarrow c\bar{c}$, $Q^2 = \hat{s}$. (Q^2 choice-1)
2. for both $gg \rightarrow c\bar{c}$ & $q\bar{q} \rightarrow c\bar{c}$, $Q^2 = \hat{s}$. (Q^2 choice-2)

We take $n_f = 4$ for charm quark production and $n_f = 5$ for bottom quark production. The QCD scale Λ depends on the choice of parton distribution functions and is given in the table below

Parton distribution functions	$\Lambda(\text{GeV})$
GRV-LO set	0.25
GRV-HO set	0.20
Duke-Owens set 1(DO1)	0.20
Duke-Owens set 2(DO2)	0.40

To incorporate approximately the next-to-leading-order corrections to the above rates we multiply the leading order results by a K-factor. In general, K-factor depends on the choice of parton distribution functions, the center of mass energy of the collision, and the type of the projectile and target particles. Calculations to order $O(\alpha_s^3)$ for the subprocesses were carried out [20,21], and afterwards the calculations to order $O(\alpha_s^3)$ for $p + p$ collisions were

made [22,23]. For DO1, $M_c = 1.5$ GeV, $Q^2 = 4M_c^2$, $P_{ab} = 100 - 1000$ GeV, the K-factor for $p - p$ collisions [22] was found to range from 2.85 to 4.1. We also note a recent result [24] where the dependence of the K-factor on the final momentum of the initially produced charm was studied for high energy AA collisions. As a function of the rapidity of the charm, the K-factor is almost a constant ~ 2 . As a function of p_\perp , the K-factor increases from 1.3 at $p_\perp = 0.7$ GeV to 3.4 at $p_\perp = 6$ GeV.

In Fig. 1 we compare the so calculated charm cross section to the limited data on inclusive $c\bar{c}$ production in $p - p$ collisions. The NA34 data for σ_{charm} is taken directly from ref. [25]. The values for the other data lines are computed from D-meson cross sections according the argument in ref. [26] by using the published experiment results [27–30]. Earlier experiment results [31] also show big uncertainties among the different experiments.

In Fig. 1 We see that both the solid curve and the dashed curve fit the low energy data reasonably well, so we use these two parametrizations for the following high energy calculations in this section. As a consistency check, we also plot the long-dashed curve using the same parameters as in Fig. 1 of ref. [22] (i.e. DO1, $M_c = 1.5$ GeV, $Q^2 = 4M_c^2$) using constant $K = 3$ for simplicity. Comparing the solid and dot-dashed curves shows the strong dependence on the assumed charm quark mass for the GRV-HO set. Comparing the solid and dashed curve we see that different choices for the Q^2 scale can be compensated for by shifts in the K factor. These results together with the large uncertainty of data emphasize the need to measure pp and pA to fix uncertainties in the initial charm production rate in order that charm production in AA can be properly calculated.

Next we compare our results for the rapidity density of produced $c\bar{c}$ pairs at $Y = 0$ with results of ref. [4]. In Fig. 2 the energy dependence in the range between RHIC and LHC ($\sqrt{s} = 200 - 6300$ AGeV) for $Au + Au$ collisions are shown. The scaling from pp results to AA is

$$\left(\frac{dN}{dY}\right)_{Y=0}^{AA} = A^{\alpha+1/3} \left(\frac{d\sigma}{dY}\right)_{Y=0}^{pp} / \sigma_{inelastic}^{pp} \quad (3)$$

where $\sigma_{inelastic}^{pp}$ is taken from ref. [32]. Glauber geometry for central high $A + A$ collisions

gives $\alpha = 1$. In Fig. 2 the solid curve is our result using the same parameters as for the solid curve in Fig. 1. The parametrization for the dashed curve in Fig. 1 gives a curve higher than the solid curve by 15% to 30%. The four long-dashed curves, curve1 to curve4, are all from PCM calculations [4]. The top curve4 is the parton cascade model result for the so-called QGP formation case, including both the fusion and the flavor excitation processes. That curve is higher than our solid curve by about an order of magnitude because it includes the contribution from flavor excitation processes. Curve3, the curve with filled squares, shows the contribution to curve4 from fusion processes only (processes (1) and (2) in the notation of ref. [4]), and curve3 is very close to our results. The bottom curve1 is the estimate without QGP formation by extrapolating the parton model pp result to AA using $A^{1.09}$ scaling. It is lower than our solid curve by a factor of 6 to 2.5. The main source of this difference is from the A -dependence of $p - A$ cross sections. Ref. [4] used an A^α scaling with $\alpha = 0.76$ [33] instead of the value $\alpha = 1$ we use from Glauber geometry. We note that the value $\alpha = 0.76$ is taken from low energy experiments, where energy conservation suppresses the contribution from multiple collisions. At high energies, QCD factorization implies that $\alpha = 1$ for $p - A$ scaling is the appropriate scaling modulo small nuclear shadowing effects. To demonstrate this effect from different A^α scaling, we multiply Curve1 by a factor of $A^{1.0}/A^{0.76} = 3.55$ and get Curve2, which is close to our results. In summary, the factor ~ 50 enhancement of charm production suggested in ref. [4] comparing curve1 with curve4 for charm production at *RHIC* is a consequence of the inclusion of incoherent flavor excitation processes and the extrapolation from pp to AA via low energy scaling. Given the coherent suppression of the flavor excitation processes [12] and the high energy scaling under consideration, it is only sensible to compare curve2 with curve3. In that case Fig. 2 leads to the expectation that the pre-equilibrium charm production should be comparable to the initial fusion rate. This removes the bulk of the discrepancy between ref. [2] and ref. [4].

As a further check on the parameters we compare charmed hadron x_f results in Fig. 3 with 400 GeV $p - p$ data [27] using the idealized δ -function fragmentation function. The realistic fragmentation function used in ref. [16] lowers the curves slightly and reveals the

true high- x_f intrinsic charm component. In Fig. 4 we compare $b\bar{b}$ production. Here we take $M_c = 4.75$ GeV as in ref. [23], with $K = 3, n_f = 5$. The data point at $\sqrt{S} = 630$ GeV is from ref. [34]: $\sigma(p\bar{p} \rightarrow b + X) = 19.3 \pm 7(\text{exp.}) \pm 9(\text{th.}) \mu\text{b}$, and only the experimental error is indicated in Fig. 4. At $\sqrt{S} = 1.8\text{TeV}$, our value is $41.8\mu\text{b} \times K = 125\mu\text{b}$. This is significantly larger than found in ref. [23].

III. PRE-EQUILIBRIUM CHARM PRODUCTION

We consider next the pre-equilibrium contribution to the charm yield in $A + A$. This is the charm produced through final state interactions between partons in the dense mini-jet plasma. Here we only calculate the dominant contribution from mini-jet gluon fusion.

A. Spectrum of Mini-Jets

The spectrum of mini-jet gluons in leading-order follows from ref. [35]

$$\frac{d\hat{\sigma}}{d\hat{t}}_{gg \rightarrow gg} = \frac{9\pi\alpha_s^2}{2\hat{s}^2} \left[3 - \frac{\hat{u}\hat{t}}{\hat{s}^2} - \frac{\hat{u}\hat{s}}{\hat{t}^2} - \frac{\hat{s}\hat{t}}{\hat{u}^2} \right] \quad (4)$$

$$\frac{d\hat{\sigma}}{d\hat{t}}_{gq \rightarrow gq} = \frac{\pi\alpha_s^2}{\hat{s}^2} \left[-\frac{4\hat{u}^2 + \hat{s}^2}{9\hat{u}\hat{s}} + \frac{\hat{u}^2 + \hat{s}^2}{\hat{t}^2} \right] \quad (5)$$

The term mini-jets refers to unresolved jets at a scale $p_\perp > p_{\perp cut} = 2\text{GeV}$. The inclusive cross section to produce mini-jets is given by

$$\frac{d\sigma}{dy dp_\perp^2} = \int dy_3 x_1 f_1 x_2 f_2 \frac{d\hat{\sigma}}{d\hat{t}} (1 + 2 \rightarrow 3 + 4) \quad (6)$$

where f_1 is the incident parton distribution evaluated at $x_1 = p_\perp(e^y + e^{y_3})/\sqrt{s}$ at a scale $Q^2 = p_\perp^2$. The light-cone coordinates of the initial and final partons are $p_1 = [2x_1 p_0, 0, \vec{0}]$, $p_2 = [0, 2x_2 p_0, \vec{0}]$, $p_3 = [m_\perp e^{y_3}, m_\perp e^{-y_3}, -\vec{p}_\perp]$, and the observed parton has $p = [m_\perp e^y, m_\perp e^{-y}, \vec{p}_\perp]$. The subprocess Mandelstam variables are $\hat{s} = sx_1 x_2$ etc.. For the calculation of mini-jet gluon fusion process in the following section III B, we choose $Q^2 = \hat{s}$. As in ref. [2], we use DO1 as the proton structure functions and $K = 2$, $M_c = 1.5\text{GeV}$

for the mini-jet production. Shadowing on Au is taken from ref. [36]. The resulting transverse momentum distribution of mid-rapidity mini-jet gluons at $\sqrt{s} = 200$ AGeV is shown by the open circles in Fig. 5. We call this distribution the hard distribution since it has $p_{\perp cut} = 2\text{GeV}$. It is compared to the solid line, which is the output of the Monte Carlo calculation via the HIJING model [8] that includes initial and final state radiation.

For convenience we have parameterized the Monte Carlo results as the following:

$$\frac{dN}{dydp_{\perp}^2} \equiv g(p_{\perp})\rho(y)A^{4/3} = 0.06e^{-1.25p_{\perp}} \cos\left[\frac{\pi(\frac{y}{3.7})^{1.8}}{2}\right]A^{4/3}, \quad \text{with } |y| \leq 3.7 \quad (7)$$

In the following, we call this parameterized distribution the soft+hard distribution. The soft+hard, hard, and Monte Carlo distributions are very close to each other in the semi-hard $p_{\perp} > 2$ GeV region at $y = 0$, as seen in Fig. 5. However the parametrized distribution falls underneath the Monte Carlo result in the region $p_{\perp} < 1$ GeV. We emphasize that the soft component is strongly model dependent as it requires the furthest extrapolation from the pQCD hard domain. The Hijing yield in that region is due to initial and final state radiation. Other contributions in this soft domain from coherent string are possible [6]. While most of the following results are obtained with the simple parametrization above, we will check the sensitivity to variations of the soft component as well. We also note that at bigger rapidity the p_{\perp} spectrum falls more rapidly. The above parametrization does not include that property. However, that property only lowers the high p_{\perp} tail, and hardly changes the low p_{\perp} part and the total number of the pre-equilibrium charm.

B. $\eta - y$ correlations

1. Bjorken correlation

In ideal Bjorken dynamics, the space-time rapidity $\eta = 1/2 \log[(t+z)/(t-z)]$ and the true momentum rapidity $y = 1/2 \log[(E + p_z)/(E - p_z)]$ are assumed to be perfectly correlated. This is referred to as the inside-outside picture and the phase-space distribution function in this case has the form

$$F(\vec{x}, \vec{p}, t)_{Bj} = \frac{(2\pi)^3}{\tau\pi R_A^2 p_\perp} \frac{dN}{dy d\vec{p}_\perp} \delta(\eta - y) \Theta(\tau - \tau_i) \Theta(\tau_f - \tau) \quad (8)$$

$\tau_i = 0.1 fm/c$ is the mini-jet formation time. $\tau_f \approx 1.7 fm/c$ is the proper time when the energy density of the pre-equilibrium mini-jets falls by an order of magnitude to $\sim 2 GeV/fm^3$ due to rapid longitudinal expansion, and that is when we terminate the pre-equilibrium stage.

The phase space distribution is normalized such that

$$\int \frac{F(\vec{x}, \vec{p}, t)_{Bj} d^3x}{(2\pi)^3} = \frac{d^3N}{d^3p} = \frac{1}{E} \frac{dN}{dy d\vec{p}_\perp} \quad (9)$$

In this section we study the pre-equilibrium charm production at $y = 0$ [2]:

$$\left(E \frac{d^3N}{d^3p} \right)_{y=0} = \int d^4x \int \frac{1}{32(2\pi)^8} \frac{d^3p_1 d^3p_2 d^3p'}{\omega_1 \omega_2 E'} F(\vec{x}, \vec{p}_1, t) F(\vec{x}, \vec{p}_2, t) |M|^2 \delta^4(\sum P^\mu) \quad (10)$$

Denoting $dN/dy d\vec{p}_\perp \equiv g(y, p_\perp)$, and $p_{\perp 1} = (\cos\phi_1, \sin\phi_1, 0)p_{\perp 1}$, the ideal η - y correlation leads to

$$\begin{aligned} \left(E \frac{d^3N}{d^3p} \right)_{y=0} &= \int_{\tau_i}^{\tau_f} \frac{d\tau}{32(2\pi)^2 \tau \pi R_A^2} \int d\eta dp_{\perp 1} dp_{\perp 2} d\phi_1 d\phi_2 \frac{g(\eta, p_{\perp 1}) g(\eta, p_{\perp 2}) \delta(\sum E) |M|^2}{E'} \\ &= \frac{\ln(\tau_f/\tau_i)}{32(2\pi)^2 \pi R_A^2} \int d\eta dp_{\perp 2} d\phi_1 d\phi_2 \frac{g(\eta, p_{\perp 1,0}) g(\eta, p_{\perp 2}) |M|^2}{p_{\perp 2} [1 - \cos(\phi_1 - \phi_2)] - (E \cosh\eta - p \cos\phi_1)} \end{aligned} \quad (11)$$

In deriving the above, we have used kinematic relations

$$\begin{aligned} E' &= (p_{\perp 1} + p_{\perp 2}) \cosh\eta - E \\ \frac{\delta(\sum E)}{E'} &= \frac{\delta(p_{\perp 1} - p_{\perp 1,0})}{p_{\perp 2} [1 - \cos(\phi_1 - \phi_2)] - (E \cosh\eta - p \cos\phi_1)} \\ p_{\perp 1,0} &= \frac{p_{\perp 2} (E \cosh\eta - p \cos\phi_2)}{p_{\perp 2} [1 - \cos(\phi_1 - \phi_2)] - (E \cosh\eta - p \cos\phi_1)} \end{aligned} \quad (12)$$

Numerical integration of the above integral in equation (11) leads to the results shown in Fig. 6. The solid line is the p_\perp -distribution for the initial charm production, from section II. We see that the pre-equilibrium contribution in this strongly correlated case is totally negligible. This result is similar to the thermal charm production contribution calculated in ref. [2] except that in our case the curve extends to higher p_\perp because of the broader initial mini-jet distribution in p_\perp .

2. Uncorrelated $\eta - y$

In ref. [2], another extreme case, opposite to the ideal Bjorken picture, was considered. In that case the gluon distribution is assumed to be completely uncorrelated as in an ideal thermal fireball. This assumption leads to

$$F(\vec{x}, \vec{p}, t)_{Fb} = \frac{(2\pi)^3}{p} \frac{1}{V} \frac{dN}{dy d\vec{p}_\perp} \quad (13)$$

If one assumes a fixed volume $V = \tau_i \pi R_A^2$, then $\int dt \sim \tau_f - \tau_i$, and

$$\int \frac{d^4x}{V^2} \sim \frac{1}{\pi R_A^2} \frac{\tau_f}{\tau_i} \quad \text{as in ref. [2]}. \quad (14)$$

Then from equation (10), we have

$$\left(E \frac{d^3N}{d^3p} \right)_{y=0} = \frac{I(p_\perp)}{32(2\pi)^2} \int \frac{d^4x}{V^2} = \frac{\tau_f/\tau_i}{32(2\pi)^2 \pi R_A^2} I(p_\perp) \quad (15)$$

where

$$\begin{aligned} I(p_\perp) &= \int \frac{dy_1 dy_2 dp_{\perp 2} d\phi_1 d\phi_2}{\cosh y_1 \cosh y_2} \frac{g(y_1, p_{\perp 1,0}) g(y_2, p_{\perp 2}) |M|^2}{p_{\perp 2} [\cosh(y_1 - y_2) - \cos(\phi_1 - \phi_2)] - (E \cosh y_1 - p \cos \phi_1)} \\ \frac{\delta(\sum E)}{E'} &= \frac{\delta(p_{\perp 1} - p_{\perp 1,0})}{p_{\perp 2} [\cosh(y_1 - y_2) - \cos(\phi_1 - \phi_2)] - (E \cosh y_1 - p \cos \phi_1)} \\ p_{\perp 1,0} &= \frac{p_{\perp 2} (E \cosh y_2 - p \cos \phi_2)}{p_{\perp 2} [\cosh(y_1 - y_2) - \cos(\phi_1 - \phi_2)] - (E \cosh y_1 - p \cos \phi_1)} \end{aligned} \quad (16)$$

For uncorrelated case, the pre-equilibrium charm production is much larger than the Bjorken-correlation case, and is comparable with the initial charm yield, as shown in Fig. 7. This is similar to the result in ref. [2] where the pre-equilibrium charm production has almost the same magnitude and p_\perp -shape as the initial charm.

3. Minimally-correlated $\eta - y$

We consider here the simplest source of $\eta - y$ correlations resulting from the minimal geometrical spread in initial production points required by the uncertainty principle. This type of correlations are included in the parton cascade model and discussed in ref. [9]. The phase space distribution function including such minimal correlations has the form

$$F(\vec{x}, \vec{p}, t)_{Min} = \mathcal{N} \int \frac{dN}{dy dp_{\perp}} \frac{\theta(\tau_{max} - \frac{t}{\cosh y})}{1 + (\frac{t_f(p)}{\Delta t})^2} \rho_0(\vec{x}_0, t_0) \delta(\vec{x} - \vec{x}_0 - \vec{v} \Delta t) d^3 x_0 dt_0 . \quad (17)$$

The integration is over the space-time coordinates (\vec{x}_0, t_0) of the production points of the gluons. These points are distributed according to a normalized density $\rho_0(\vec{x}_0, t_0)$. The delta function arises to take into account the free streaming of the partons from the production point, with velocity $\vec{v} = \vec{p}/E$, where $E = p_{\perp} \cosh y$ and $p_z = p_{\perp} \sinh y$. The theta function defines what we mean by pre-equilibrium. The proper time when the pre-equilibrium fusion is terminated is τ_{max} , which is determined below in Fig. 8. The theta function insures that only those gluons with proper time less than τ_{max} contribute.

The formation physics is included via the Lorentzian formation factor [10]

$$[1 + (t_f(p)/\Delta t)^2]^{-1} , \quad (18)$$

where $\Delta t = t - t_0$ is the elapsed time, and the formation time is given by

$$t_f(p) \simeq \cosh y \frac{0.2 \text{GeV}}{p_{\perp}} (fm) . \quad (19)$$

We note that the above formation factor more accurately describes the interference phenomena suppressing production at early time than the conventionally assumed factor

$$\theta[\Delta t - t_f(p)] . \quad (20)$$

In the following we consider both formation functions for comparison to check for the sensitivity to this formation physics.

We assume that $\int \rho_0(\vec{x}_0, t_0) d^3 x_0 dt_0 = 1$. In this case the normalization factor is $\mathcal{N} = (2\pi)^3/E$, so that

$$\lim_{t \rightarrow \infty} \int F(\vec{x}, \vec{p}, t)_{Min} d^3 x / (2\pi)^3 = d^3 N / d^3 p . \quad (21)$$

As discussed in ref. [9], the production points are spread along the beam axis according to the uncertainty principle by an amount $\delta z \equiv d \sim \hbar/p_{\perp}$ since the dominant parton interaction leading to a $y = 0$ parton with final p_{\perp} has an initial longitudinal momentum $xP_0 \sim p_{\perp}$.

We take as a particular model

$$d = \frac{0.2}{p_{\perp}}(fm) \quad (22)$$

Clearly this is only a rough guess, but it allows us at least to investigate the sensitivity of the results to a particular $\eta - y$ correlation that results from this spatial spreading of the production points. We emphasize that it is precisely the uncertainty of the initial space-time formation physics that leads us to study the possibility of open charm production as an experimental probe of that physics.

Given the above assumption we take

$$\rho_0(\vec{x}_0, t_0) = \frac{1}{\pi R_A^2} \delta(t_0) \frac{e^{-z_0^2/(2d^2)}}{\sqrt{2\pi}d} \quad (23)$$

where d is the mean spread for gluons depending on p_{\perp} from above. This distribution only spreads out the production points along the beam axis. A more realistic treatment would also smear out in the time coordinate.

Neglecting transverse expansion, we obtain finally

$$F(\vec{x}, \vec{p}, t)_{Min} = \frac{(2\pi)^3}{\sqrt{2\pi}\pi R_A^2} \frac{p_{\perp}}{0.2} e^{-(z - \tanh y t)^2 (\frac{p_{\perp}}{0.2})^2/2} \frac{1}{p} \frac{dN}{dy dp_{\perp}} \frac{\theta(\tau_{max} - \frac{t}{\cosh y})}{1 + (\frac{0.2 \cosh y}{p_{\perp} t})^2} \quad (24)$$

Let $a_1 = \tanh y_1$, $a_2 = \tanh y_2$, $b_1 = (\frac{p_{\perp 1,0}}{0.2})^2/2$, $b_2 = (\frac{p_{\perp 2}}{0.2})^2/2$, then after integration over z , we have the final expression as the following, while its numerical results are shown in Fig. 9:

$$\left(E \frac{d^3 N}{d^3 p} \right)_{y=0} = \frac{\sqrt{\pi}}{16(2\pi)^4 R_A^2} \int dy_2 dy_1 dp_{\perp 2} d\phi_2 d\phi_1 \frac{p_{\perp 1,0} \frac{p_{\perp 1,0}}{0.2} \frac{p_{\perp 2}}{0.2} |M|^2}{p_{\perp 2} \cosh y_1 \cosh y_2 (E \cosh y_2 - p \cos \phi_2)} \frac{g(y_1, p_{\perp 1,0}) g(y_2, p_{\perp 2})}{\sqrt{b_1 + b_2}} \int_0^{t_f} dt \frac{e^{-\frac{(a_1 - a_2)^2 t^2}{1/b_1 + 1/b_2}}}{\left[1 + \left(\frac{0.2 \cosh y_1}{p_{\perp 1,0} t} \right)^2 \right] \left[1 + \left(\frac{0.2 \cosh y_2}{p_{\perp 2} t} \right)^2 \right]} \quad (25)$$

In the above $t_f = \tau_{max} \min(\cosh y_1, \cosh y_2)$, and $p_{\perp 1,0}$ is the same as in equation (16). Note that by using the unit GeV for momentum and unit fm for time, the expression $\left(E \frac{d^3 N}{d^3 p} \right)_{y=0}$ in equations (11), (15), and (25) has the dimension $GeV^{-4} fm^{-2}$, and we need a factor $(\hbar c)^2 \sim (0.2 GeV fm)^2$ to convert it to the dimension GeV^{-2} , which we have used in Fig. 6, Fig. 7, Fig. 9 and Fig. 10.

We also plot the energy density curve at $z = 0$ as a function of time in Fig. 8. We see that it increases first, and reaches maximum at the time about $0.1 fm/c$, then the energy

density decreases linearly to $\sim 2\text{GeV}/fm^3$ at $\sim 0.9fm/c$ ($1.7fm/c$) for hard (soft+hard) distribution. We choose the above time as the cutoff τ_{max} .

The previous uncorrelated case neglects the finite formation times of the mini-jets. In order to see the formation-time effect, we also use the θ -function form in equation (20) instead of the Lorentzian form in equation (18) for the formation-time effect. The result from this θ -function is about 10% higher at $p_{\perp} = 0\text{GeV}$, and 10% lower at $p_{\perp} = 9\text{GeV}$, as shown in Fig. 10. The lack of sensitivity to the formation-time physics is due to the relative large p_{\perp} for the gluon mini-jets in the charm production process. There would be more sensitivity had the production been dominated by low p_{\perp} components.

We also see that for the soft+hard distribution the soft gluons significantly increase the pre-equilibrium charm production in both low- p_{\perp} and high- p_{\perp} region, with the largest increase in low- p_{\perp} region. It is interesting to identify where the enhancement comes from. In Fig. 9, the curve with diamonds shows the contribution from the fusion of soft gluons both with $p_{\perp} < 2\text{ GeV}$, and the curve with unfilled squares shows the contribution from the fusion of hard gluons both with $p_{\perp} > 2\text{ GeV}$. These two curves are both very low compared with the curve calculated from the soft+hard distribution. So the enhancement going from hard distribution to soft+hard distribution mainly comes from the fusion of hard and soft mini-jet gluons.

We have noted before that our fit for the mini-jet gluon spectrum falls below the Monte Carlo result from HIJING calculation. We can fit the soft gluons from HIJING better by using $0.265e^{-2.6p_{\perp}}$ for $p_{\perp} \in (0, 1.1)\text{ GeV}$, and use the old fit $0.06e^{-1.25p_{\perp}}$ for higher- p_{\perp} gluons. This new fit gives us more very soft gluons. We have done the calculation for minimally-correlated case using the new fit, and the result is different only by less than 10%, which means the super-soft gluons are not very important for the pre-equilibrium charm production.

There is also a possible cross-term contribution from the interactions of the incoming nuclei and the pre-equilibrium gluon mini-jets. However, our preliminary result shows that it is not larger than the above pre-equilibrium charm yield and is therefore also negligible

compared with the initial charm production.

C. Why is the pre-equilibrium charm yield so small?

To understand the reason why the pre-equilibrium charm yield is so small compared to the initial yield as found through tedious numerical calculations in the previous section, we consider here the calculation of the total number of pre-equilibrium charm pairs. The expression for that number is given by

$$N = \frac{(\hbar c)^2}{4(2\pi)^6} \int d^4x \int \frac{d^3p_1}{\omega_1} \frac{d^3p_2}{\omega_2} F(\vec{x}, \vec{p}_1, t) F(\vec{x}, \vec{p}_2, t) \hat{\sigma}(\hat{s}) \quad (26)$$

where $\hat{\sigma}(\hat{s})$ is the integrated cross section for the process $gg \rightarrow c\bar{c}$, see equation(2). Our main strategy is to estimate the mean difference between the two gluon rapidities, then from the kinematical constraint on charm production ($\hat{s} \geq 4M_c^2$) estimate the effective lower cutoff for p_\perp of the mini-jet gluons. Thus we separate the p_\perp integrals from the rapidity integrals. and have a rough estimate for the total number of charm pairs.

1. Bjorken correlation case and Uncorrelated case

For the fireball case,

$$F(\vec{x}, \vec{p}, t)_{Fb} = \frac{(2\pi)^3}{p} \frac{1}{V} \frac{dN}{dy dp_\perp} \\ \hat{s} = 2p_{\perp 1} p_{\perp 2} [\cosh(y_1 - y_2) - \cos(\phi_1 - \phi_2)] \quad (27)$$

For the Bjorken case,

$$F(\vec{x}, \vec{p}, t)_{Bj} = \frac{(2\pi)^3}{p_\perp} \frac{dN}{dy dp_\perp} \frac{\delta(\eta - y)}{\tau \pi R_A^2} \Theta(\tau - \tau_i) \Theta(\tau_f - \tau) \\ \hat{s} = 2p_{\perp 1} p_{\perp 2} [1 - \cos(\phi_1 - \phi_2)] \quad (28)$$

For all the cases, we use the fit to the gluon distribution given by equation(7), where $g(p_\perp) \equiv ae^{-bp_\perp} = 0.06e^{-1.25p_\perp}$. Therefore,

$$\begin{aligned}
N_{Fb} &= \frac{(\hbar c)^2 \frac{\tau_f}{\tau_i} A^{8/3}}{4\pi R_A^2} \int dy_1 \frac{\rho(y_1)}{\cosh y_1} \int dy_2 \frac{\rho(y_2)}{\cosh y_2} \int dp_{\perp 1} g(p_{\perp 1}) \int dp_{\perp 2} g(p_{\perp 2}) \int d\phi_1 \int d\phi_2 \hat{s}\hat{\sigma}(\hat{s}) \\
N_{Bj} &= \frac{(\hbar c)^2 \ln \frac{\tau_f}{\tau_i} A^{8/3}}{4\pi R_A^2} \int d\eta [\rho(\eta)]^2 \int dp_{\perp 1} g(p_{\perp 1}) \int dp_{\perp 2} g(p_{\perp 2}) \int d\phi_1 \int d\phi_2 \hat{s}\hat{\sigma}(\hat{s})
\end{aligned} \tag{29}$$

The dominant contribution is coming from the vicinity of the production threshold where $\hat{s} = 4M_c^2 = 9\text{GeV}^2$ [11], so we make the following rough estimates:

$$\begin{aligned}
\hat{s}\hat{\sigma}(\hat{s}) &\sim \alpha^2(\hat{s}) \sim 0.06 \\
\int dp_{\perp} g(p_{\perp}) &\sim \int_{p_c}^{\infty} dp_{\perp} g(p_{\perp}) \sim \frac{a}{be^{bp_c}}
\end{aligned} \tag{30}$$

where p_c is the effective cutoff value for $p_{\perp 1}$ and $p_{\perp 2}$ from the requirement $\hat{s} \geq 4M_c^2$.

For the fireball case,

$$\langle \cosh(y_1 - y_2) \rangle \equiv \frac{\int dy_1 dy_2 \frac{\rho(y_1)}{\cosh y_1} \frac{\rho(y_2)}{\cosh y_2} \cosh(y_1 - y_2)}{\int dy_1 dy_2 \frac{\rho(y_1)}{\cosh y_1} \frac{\rho(y_2)}{\cosh y_2}} \sim 4.0 \tag{31}$$

Since the mini-jet p_{\perp} spectrum is dropping almost exponentially, the production heavily favors the smaller cutoff p_c , so the mean value of $\cos(\phi_1 - \phi_2)$ is most likely to be negative. We take $\langle \cos(\phi_1 - \phi_2) \rangle \sim -0.5$. Then $\hat{s} \sim 9p_c^2$, so the effective cutoff for the fireball case is $p_c \sim 1.0$ GeV.

On the other hand, for the Bjorken case,

$$y_1 = y_2 = \eta \Rightarrow \hat{s} \sim 3p_c^2 \Rightarrow p_c \sim 1.73\text{GeV} \tag{32}$$

Using the same values as in section III B: $\tau_i = 0.1fm$, $\tau_f = 1.0fm$ for fireball case, $\tau'_f = 1.7fm$ for Bjorken case, and

$$\int dy_1 \frac{\rho(y_1)}{\cosh y_1} \sim 2.8, \quad \int d\eta [\rho(\eta)]^2 \sim 4.9 \tag{33}$$

We then have the estimate for the total number of the pre-equilibrium charm:

$$\begin{aligned}
N_{Fb} &\sim \frac{(\hbar c)^2 \frac{\tau_f}{\tau_i} A^{8/3}}{4\pi R_A^2} 2.8^2 \left(\frac{a}{be^{1.0b}}\right)^2 (2\pi)^2 [\hat{s}\hat{\sigma}(\hat{s})] \sim 3.5 \\
N_{Bj} &\sim \frac{(\hbar c)^2 \ln \frac{\tau'_f}{\tau_i} A^{8/3}}{4\pi R_A^2} 4.9 \left(\frac{a}{be^{1.73b}}\right)^2 (2\pi)^2 [\hat{s}\hat{\sigma}(\hat{s})] \sim 0.098
\end{aligned} \tag{34}$$

Therefore we estimate $N_{Fb}/N_{Bj} \sim 35$, in rough agreement with the detailed numerics. We see that the main source of the large increase going from the Bjorken case to the fireball case comes from the different p_{\perp} cutoff. In the uncorrelated fireball case, one allows particles with different rapidities to interact with each other (see equation(31)), thus more low p_{\perp} gluons can take part in the interaction. Since the mini-jet p_{\perp} spectrum is dropping almost exponentially, the fireball case produces a lot more pre-equilibrium charm than the Bjorken case (a factor of 6 increase from the smaller p_{\perp} cutoff). Although the questionable linear proper time dependence in the fireball case also gives an considerable increase (about a factor of 3.5), it is not as important as the correlation effect.

2. Minimal correlation case

For the minimal correlation case, the estimate is unfortunately not as straightforward. The phase space distribution function is

$$F(\vec{x}, \vec{p}, t)_{Min} = \frac{(2\pi)^3}{\sqrt{2\pi}\pi R_A^2} \frac{e^{-(z - \tanh y t)^2 (\frac{p_{\perp}}{\hbar c})^2/2}}{\hbar c \cosh y} \frac{dN}{dy d\vec{p}_{\perp}} \theta(\tau_{max} - \frac{t}{\cosh y}) \theta(\frac{\hbar c \cosh y}{p_{\perp}} - \tau_{max}) \quad (35)$$

and \hat{s} is the same as in equation(27). In the above distribution function we choose to use the θ -function for the formation-time effect. We have seen from Fig. 10 that Lorentzian formation-time formula and θ -function formula give almost the same result.

Using equation(26) and after the integration over z , we have

$$N_{Min} = \frac{(\hbar c)^2 A^{8/3}}{4\pi R_A^2 \sqrt{\pi}} \int dp_{\perp 1} g(p_{\perp 1}) \int dp_{\perp 2} g(p_{\perp 2}) \int d\phi_1 \int d\phi_2 \\ \times \int dy_1 \frac{\rho(y_1)}{\cosh y_1} \int dy_2 \frac{\rho(y_2)}{\cosh y_2} \hat{s} \hat{\sigma}(\hat{s}) \int_{t_{min}}^{t_{max}} dt \frac{e^{-\frac{(a_1 - a_2)^2 t^2}{1/b_1 + 1/b_2}}}{\sqrt{1/b_1 + 1/b_2}} \quad (36)$$

where

$$t_{min} = \hbar c \max\left(\frac{\cosh y_1}{p_{\perp 1}}, \frac{\cosh y_2}{p_{\perp 2}}\right), t_{max} = \tau_f \min(\cosh y_1, \cosh y_2) \quad (37)$$

and a_1, a_2, b_1, b_2 are defined the same as in equation(24).

We estimate that for the dominant part of the integral

$$\frac{1}{b_1} + \frac{1}{b_2} \sim \left(\frac{2\hbar c}{p_c} \right)^2, t_{min} \sim \frac{\hbar c \cosh \bar{y}}{p_c}, t_{max} \sim \tau_f \cosh \bar{y} \quad (38)$$

where $\bar{y} = (|y_1| + |y_2|)/2$. Now let $u = t p_c / (\hbar c \cosh \bar{y})$, then the last 3-dimensional integral in equation(36) without the factor $\hat{s}\hat{\sigma}(\hat{s})$ is

$$J \sim \int dy_1 \frac{\rho(y_1)}{\cosh y_1} \int dy_2 \frac{\rho(y_2)}{\cosh y_2} \frac{1}{2} \cosh \bar{y} \int_1^{\frac{\tau_f p_c}{\hbar c}} du e^{-\left[\frac{\sinh(y_1 - y_2) \cosh \bar{y}}{2 \cosh y_1 \cosh y_2} \right]^2 u^2} \quad (39)$$

The u -integral gives a dependence on τ_f which is similar to the logarithmic dependence in the Bjorken case, and the exponential form in the integrand forces the spread $y_1 - y_2$ to be small. Numerically, by taking $\tau_f \sim 1.7 fm/c$, $p_c \sim 2.0$ GeV (as the first-step value) in the u -integral, the above 3-dimensional integral is $J \sim 19.1$, and when the integrand is weighed by $\cosh(y_1 - y_2)$, the integral is ~ 23.3 . So

$$\langle \cosh(y_1 - y_2) \rangle \sim 23.3/19.1 \sim 1.22 \Rightarrow \hat{s} \sim 3.44 p_c^2 \Rightarrow p_c \sim 1.62 \text{ GeV} \quad (40)$$

Note that the above determined value of p_c is insensitive to the first-step p_c value we tried in the u -integral.

Therefore for the total pre-equilibrium charm number,

$$\begin{aligned} N_{Min} &\sim \frac{(\hbar c)^2 A^{8/3}}{4\pi R_A^2 \sqrt{\pi}} \int dp_{\perp 1} g(p_{\perp 1}) \int dp_{\perp 2} g(p_{\perp 2}) \int d\phi_1 \int d\phi_2 J \hat{s}\hat{\sigma}(\hat{s}) \\ &\sim \frac{(\hbar c)^2 A^{8/3}}{4\pi R_A^2} \frac{J}{\sqrt{\pi}} \left(\frac{a}{b e^{1.62b}} \right)^2 (2\pi)^2 [\hat{s}\hat{\sigma}(\hat{s})] \sim 0.10 \end{aligned} \quad (41)$$

Therefore $N_{Min}/N_{Bj} \sim 1$. From the above estimate we can see that although the minimally-correlated case allows particles with different rapidities to interact, the dominant contribution still comes from the region where the two gluons have almost the same rapidity, thus there is no sizeable enhancement in the pre-equilibrium charm yield. The Minimally-Correlated case is very much like the Bjorken case in that the dominant contribution comes from $y_1 \simeq y_2$ region.

As a comparison to the above rough estimates in this section, the numerical integration gives $N_{Fb} = 3.8$, $N_{Bj} = 0.093$, and $N_{Min} = 0.078$, so $N_{Min}/N_{Bj} \sim 80\%$.

IV. DISCUSSION AND SUMMARY

In this paper, we calculated initial and pre-equilibrium charm production in nuclear collisions to test the sensitivity of this probe to the unknown initial conditions in such reactions. For the initial charm production, the sensitive dependence on the choice of structure functions, the Q^2 scale, and the K-factor was noted. The parameters were fixed by fitting the limited available experimental data at lower energies. We emphasized the need for new measurements of pp and pA charm production to reduce the present large theoretical uncertainties. We argued that the copious charm production predicted in ref. [4] was mainly due to the neglect of the coherent suppression of flavor excitation processes. Our calculated initial charm yields are close to those computed in ref. [2] and to the curve 2 in Fig. 2 from ref. [4].

For the contribution from pre-equilibrium charm production, we studied the effect of correlations between the rapidity y and space-time rapidity η of mini-jet gluons. For the ideal Bjorken-correlated case, where $\eta = y_1 = y_2$, the pre-equilibrium charm production is negligible compared with the yield due to initial gluon fusion. For the opposite extreme fireball case, corresponding to uncorrelated y and η , the pre-equilibrium charm production is almost a factor of 50 larger than in the Bjorken-correlated case and is comparable with the initial charm yield [2]. By the estimates of the total pre-equilibrium charm number, we found the the difference mainly comes from the $\eta - y$ correlation. Therefore, the pre-equilibrium charm production is very sensitive to the $(\eta - y)$ correlations in the initial state.

In order to investigate the effect of more realistic correlations that may exist in the initial mini-jet plasma, we introduced a minimal correlation model taking into account the uncertainty principle along the lines of ref. [9]. Our main result is that this minimal correlation is similar to the ideal Bjorken correlation case and produces negligible pre-equilibrium charm compared with the initial charm yield. We also found that the pre-equilibrium charm yield is rather insensitive to the formation physics because the early-formed $p_{\perp} > 1$ GeV gluons dominate.

Acknowledgements: We thank K. Geiger, B. Müller, X.N. Wang, L. Xiong for useful discussions and A. Mueller for bringing refs. [12,17] to our attention.

REFERENCES

- [1] E.V. Shuryak, Phys. Lett. B78, 150 (1978).
- [2] B. Müller and X. N. Wang, Phys. Rev. Lett. 68, 2437 (1992).
- [3] E. Shuryak and L. Xiong, Phys. Rev. Lett. 70, 2241 (1993).
- [4] K. Geiger, Phys. Rev. D48, 4129 (1993).
- [5] E. Shuryak, Phys. Rev. Lett. 68, 3270 (1992).
- [6] K.J. Eskola and M. Gyulassy, Phys. Rev. C47, 2329 (1993); M. Gyulassy, K.J. Eskola, A.V. Selikhov and X.N. Wang, *in* CCAST Symposium Proceedings, Vol 10, eds Y. Pang, J. Qiu, Z. Qiu (Gordon and Breach, Amsterdam, 1994) 393.
- [7] T. Matsui and H. Satz, Phys. Lett. B178, 416 (1986); S. Gavin, H. Satz, R.L. Thews and R. Vogt, Z. Phys. C61, 351 (1994).
- [8] X.N. Wang and M. Gyulassy, Phys. Rev. D44, 3501 (1991); D45, 844 (1992).
- [9] K. Geiger and B. Müller, Nucl. Phys. B369, 600 (1992).
- [10] M. Gyulassy and X.N. Wang, Nucl. Phys. B420, 583 (1994).
- [11] B. L. Combridge, Nucl. Phys. B151, 429 (1979).
- [12] J. C. Collins, D. E. Soper and G. Sterman, Nucl. Phys. B263, 37 (1986).
- [13] R. K. Ellis, FERMILAB-CONF-86/35-T, Apr 1986. 17pp.
- [14] E. Hoffmann and R. Moore, Z. Phys. C20, 71 (1983).
- [15] G. Ingelman, L. Jönsson and M. Nyberg, Phys. Rev. D47, 4872 (1993).
- [16] R. Vogt, S. J. Brodsky and P. Hoyer, Nucl. Phys. B383, 643 (1992).
- [17] S. J. Brodsky, P. Hoyer, A. H. Mueller and W. K. Tang, Nucl. Phys. B369, 519 (1992).
- [18] M. Glück, E. Reya and A. Vogt, Z. Phys. C48, 471 (1990).

- [19] D. W. Duke and J. F. Owens, Phys. Rev D30, 49 (1984).
- [20] P. Nason, S. Dawson and R. K. Ellis, Nucl. Phys. B 303 (1988) 607; Nucl. Phys. B327, 49 (1989).
- [21] W. Beenakker, H. Kuijf, W. L. van Neerven and J. Smith, Phys. Rev. D40, 54 (1989);
W. Beenakker, W. L. van Neerven, R. Meng, G. Schuler and J. Smith, Nucl. Phys. B351, 507 (1991).
- [22] E. L. Berger, *in* Proc. Advanced Workshop on QCD Hard Processes, St. Croix, 1988.
- [23] E. L. Berger and R. Meng, Phys. Rev. D46, 169 (1992).
- [24] I. Sarcevic and P. Valerio, Phys. Lett. B338, 426 (1994).
- [25] S. Aoki et al., Phys. Lett. B224, 441 (1989).
- [26] A. T. Goshaw, *in* Proc. Advanced Workshop on QCD Hard Processes, St. Croix, 1988.
- [27] M. Aguilar-Benitez et al., Phys. Lett. B189, 476 (1987).
- [28] R. Ammar et al., Phys. Rev. Lett. 61, 2185 (1988).
- [29] K. Kodama et al., Phys. Lett. B263, 573 (1991).
- [30] M. J. Leitch et al., Phys. Rev. Lett. 72, 2542 (1994).
- [31] . S. P. K. Tavernier, Rep. Prog. Phys. 50, 1439 (1987).
- [32] K. Goulianos, *in* Physics Simulations at High Energies, edited by V. Barger et al., World Scientific, Singapore, 1987.
- [33] H. Cobbaert et al., Phys. Lett. B206, 546 (1987). M. E. Duffy et al., Phys. Rev. Lett. 55, 1816 (1985).
- [34] UA1 Collaboration, C. Albajar et al., Phys. Lett. B256, 121 (1991).
- [35] L. Combridge, J.Kripfganz and J. Ranft, Phys. Lett. 70, 234 (1977).

[36] K.J. Eskola, Nucl. Phys. B400, 240 (1993).

FIGURE CAPTIONS

Fig.1 The cross section for $pp \rightarrow c\bar{c}X$ is plotted as a function of P_{lab} . The solid line is our result with $M_c = 1.3$ GeV, $K = 3$, Q^2 choice-1 and GRV-HO set. The long-dashed curve is the result with the same parameters as in Fig. 1 of [22], but using a K-factor of 3 instead of doing $O(\alpha_s^2)$ calculation.

Fig.2 $(dN_{c\bar{c}}/dY)_{Y=0}$, rapidity density of charm and anticharm pairs for $Au - Au$ collisions vs \sqrt{S}/A . Curves 1-4 from the calculation of Parton Cascade model [4] are compared to our calculation of the yield (the solid line) due to initial fusion processes. The top curve4 is the total charm production with QGP formation including the incoherent flavor excitation processes. Curve3 shows the charm production in the case of QGP formation without excitation processes. The bottom curve1 is the parton model result extrapolated to AA from pp using the $A^{0.76}$ scaling measured at much lower energies. Curve2 is the parton model result scaled by $A^{4/3}$. Our curve uses the asymptotic $A^{4/3}$ scaling. As shown by the two arrows, curve4 becomes curve3 when the coherent cancellation of flavor excitation processes is considered, and curve1 becomes curve2 when the high energy scaling is used. So the net dynamical enhancement in the PCM (by comparing curve3 to curve2) is comparable to the result of ref. [2].

Fig.3 The production of charmed hadrons as a function of x_f for $p-p$ collisions at $P_{lab} = 400$ GeV [27]. The solid curve is our result for $d\sigma/dx_f$ using the first parameterization. The dashed curve is our result using the second parameterization. These curves assume a delta function charm fragmentation function.

Fig.4 The cross section for $p\bar{p} \rightarrow b\bar{b} + X$ vs \sqrt{S}/A . The data point at $\sqrt{S} = 630$ GeV is from ref. [34]. The dashed cross at $\sqrt{S} = 1.8$ TeV is obtained indirectly from [23], and the error bar is only illustrative.

Fig.5 The mini-jet gluon distribution $A^{-4/3} (dN/dydp_{\perp}^{\vec{r}})_{y=0}$ is plotted. The solid curve is

taken from the HIJING calculation with radiation effects included, and the circles are our result from the initial production. The dashed line is the fit $0.06e^{-1.25p_{\perp}}$.

Fig.6 The distribution $(Ed^3N/d^3p)_{y=0}$ of charm quark production using $\delta(\eta-y)$ -correlation is plotted as a function of p_{\perp} . The solid curve is the initial charm production. The curve labelled with filled diamonds is the pre-equilibrium contribution including both the soft ($p_{\perp} < 2$ GeV) and hard ($p_{\perp} > 2$ GeV) components of the mini-jet gluons. The curve labelled with unfilled diamonds is the pre-equilibrium contribution including only the hard component.

Fig.7 The distribution $(Ed^3N/d^3p)_{y=0}$ of charm quark production for the Uncorrelated case is plotted as a function of p_{\perp} . The solid curve is the initial charm production. The curve labelled with filled circles is the pre-equilibrium contribution including both the soft ($p_{\perp} < 2$ GeV) and hard ($p_{\perp} > 2$ GeV) components. The curve labelled with unfilled circles is the pre-equilibrium contribution including only the hard component.

Fig.8 The energy density at $z = 0$ is plotted as a function of proper time assuming minimal correlations and Lorentzian formation probability. The solid curve includes both soft and hard components while the dashed curve is calculated using the hard distribution and includes only the hard component.

Fig.9 The distribution $(Ed^3N/d^3p)_{y=0}$ of charm quark production using minimal $\eta - y$ correlations is plotted as a function of p_{\perp} . The curve labelled with filled squares include both components while that labelled with unfilled squares include only the fusion of hard gluons. The curve labelled with diamonds shows the contribution from fusion of soft gluons both with $p_{\perp} < 2$ GeV. This shows that the pre-equilibrium contribution mainly comes from the fusion of soft and hard gluons.

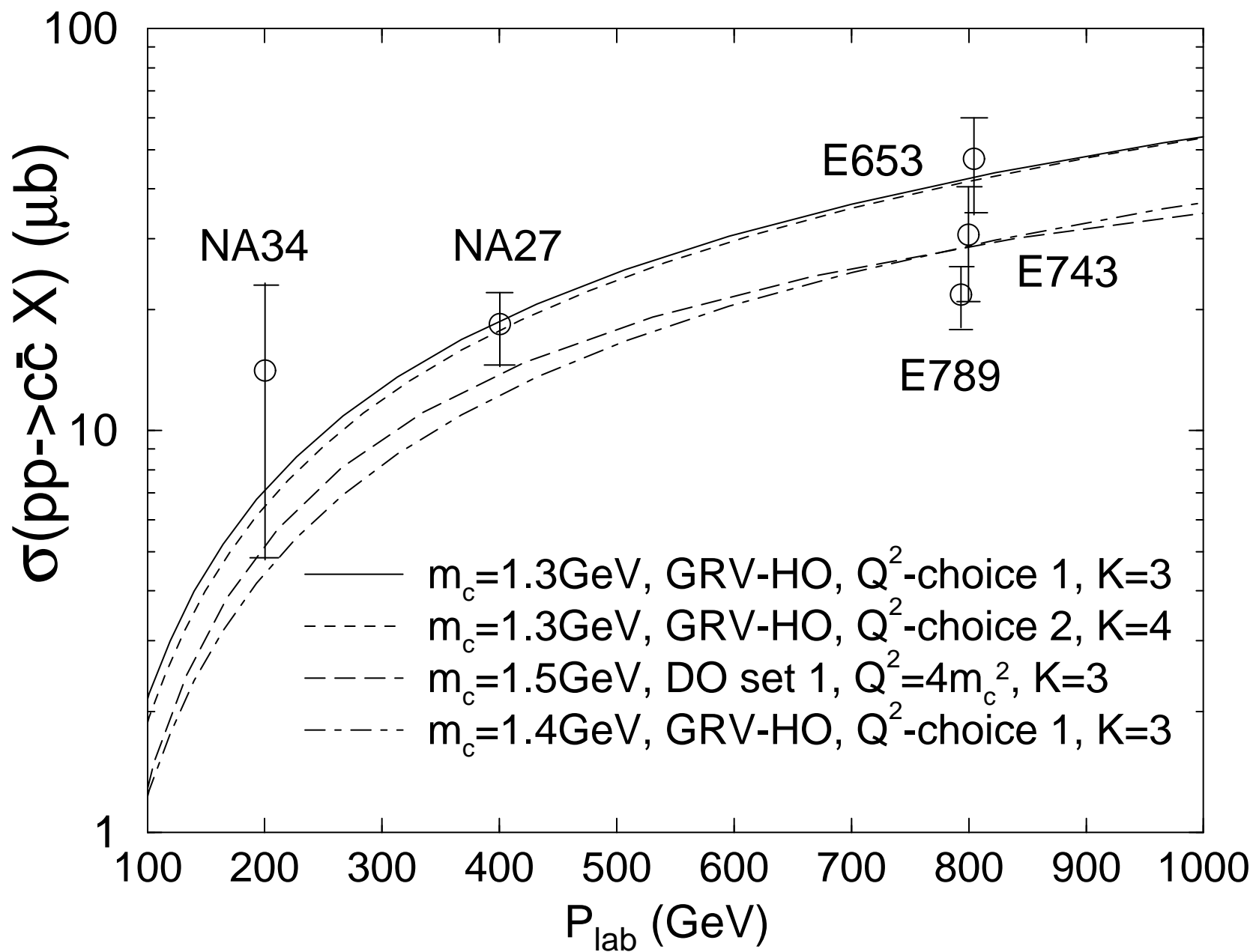
Fig.10 The distribution $(Ed^3N/d^3p)_{y=0}$ of charm quark production using different formation-time probability distributions. The solid curve is obtained using the

Lorentzian form in equation (18), and the dashed curve using the theta function form in equation (20).

This figure "fig1-1.png" is available in "png" format from:

<http://arxiv.org/ps/nucl-th/9409007v5>

Fig. 1



This figure "fig2-1.png" is available in "png" format from:

<http://arxiv.org/ps/nucl-th/9409007v5>

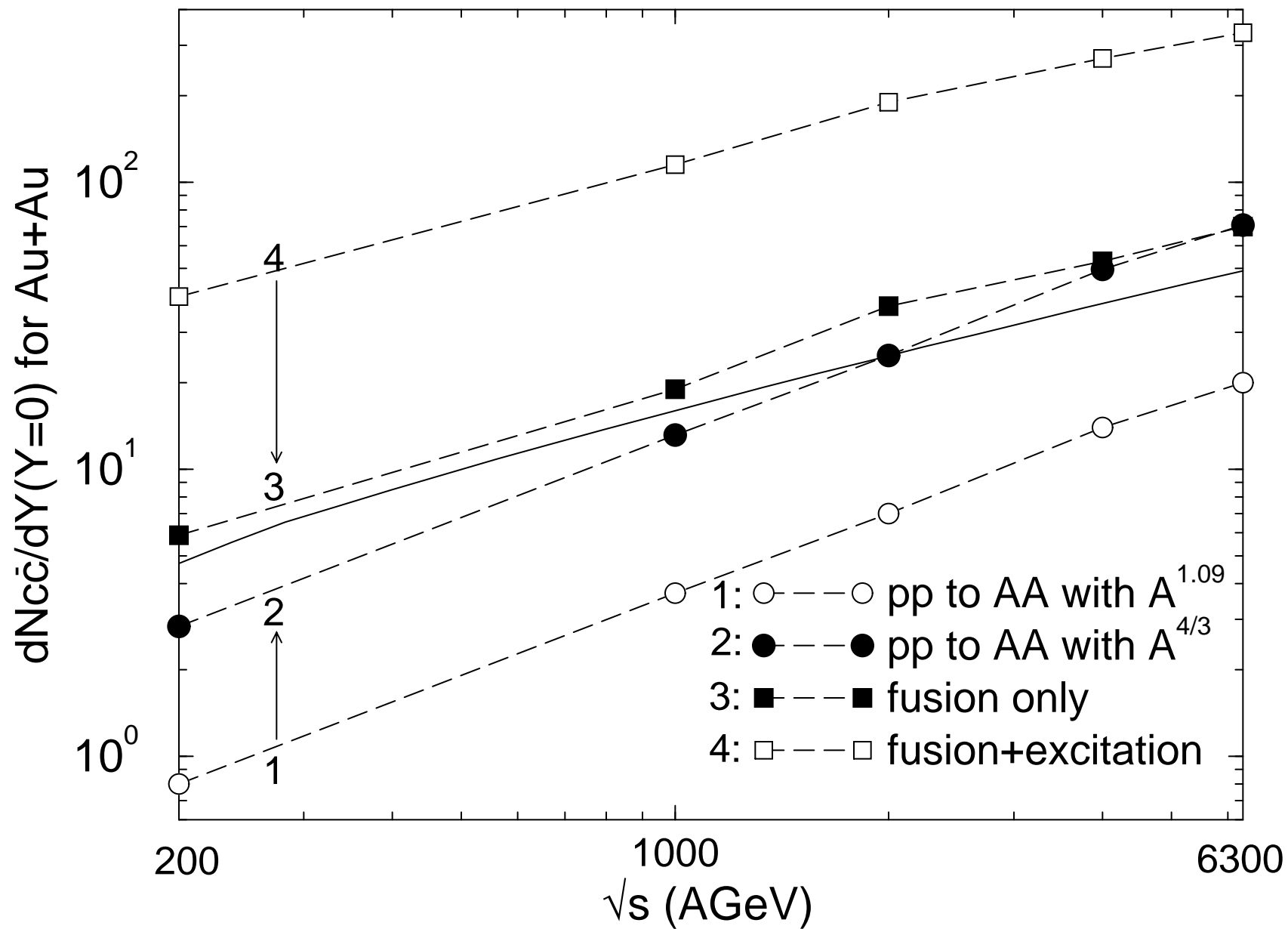
This figure "fig1-2.png" is available in "png" format from:

<http://arxiv.org/ps/nucl-th/9409007v5>

This figure "fig2-2.png" is available in "png" format from:

<http://arxiv.org/ps/nucl-th/9409007v5>

Fig. 2



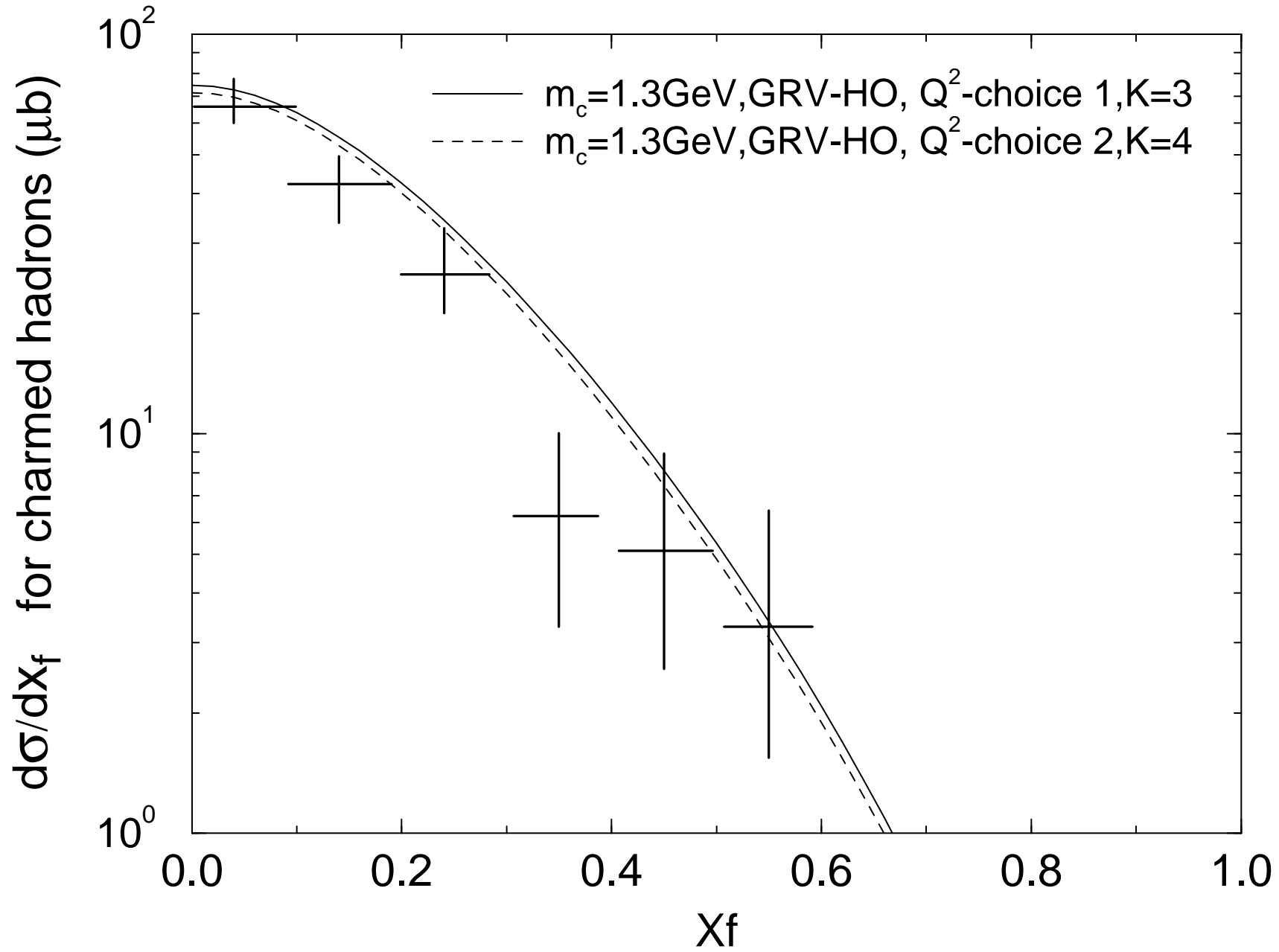
This figure "fig1-3.png" is available in "png" format from:

<http://arxiv.org/ps/nucl-th/9409007v5>

This figure "fig2-3.png" is available in "png" format from:

<http://arxiv.org/ps/nucl-th/9409007v5>

Fig. 3



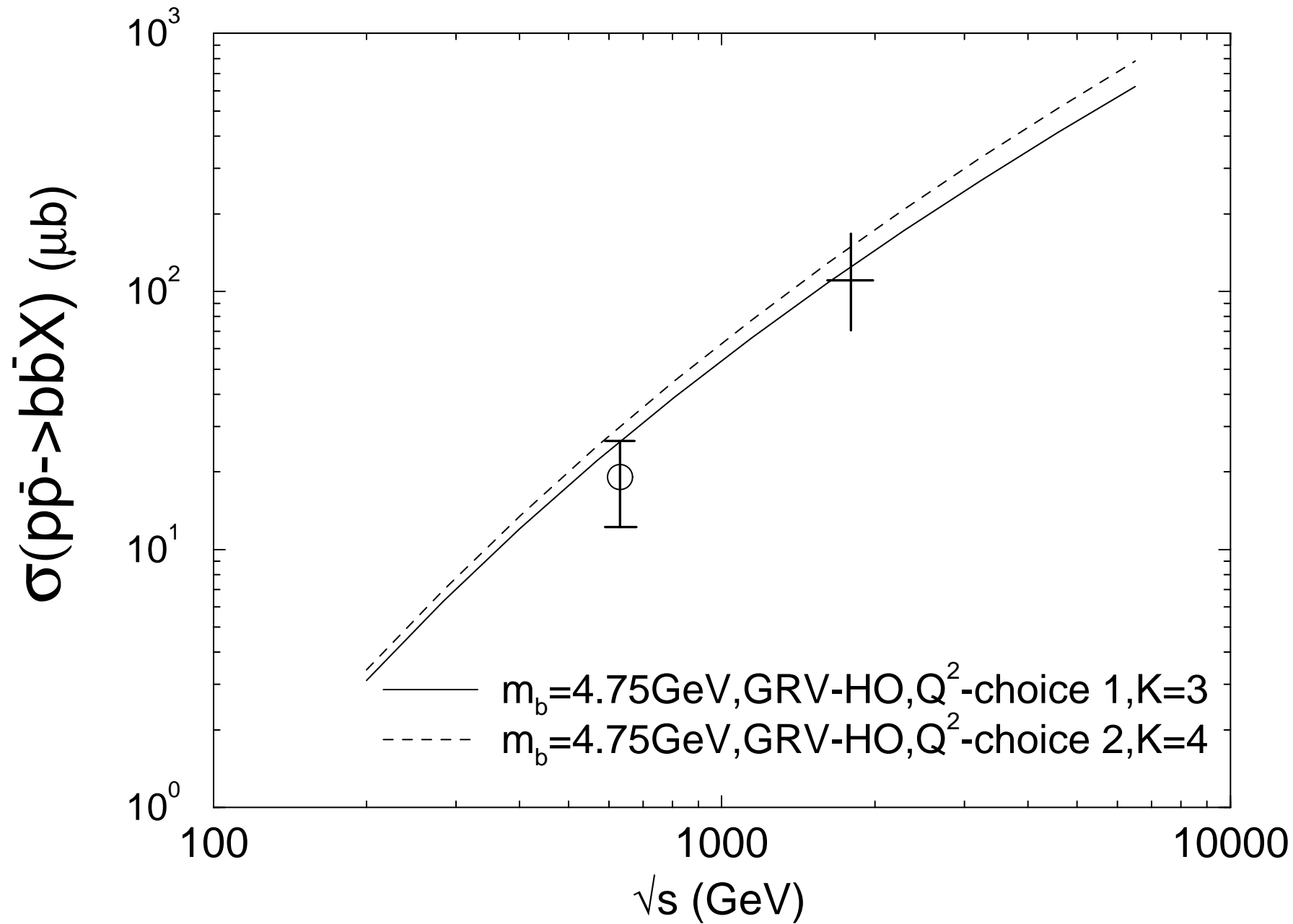
This figure "fig1-4.png" is available in "png" format from:

<http://arxiv.org/ps/nucl-th/9409007v5>

This figure "fig2-4.png" is available in "png" format from:

<http://arxiv.org/ps/nucl-th/9409007v5>

Fig. 4



This figure "fig2-5.png" is available in "png" format from:

<http://arxiv.org/ps/nucl-th/9409007v5>

Fig. 5

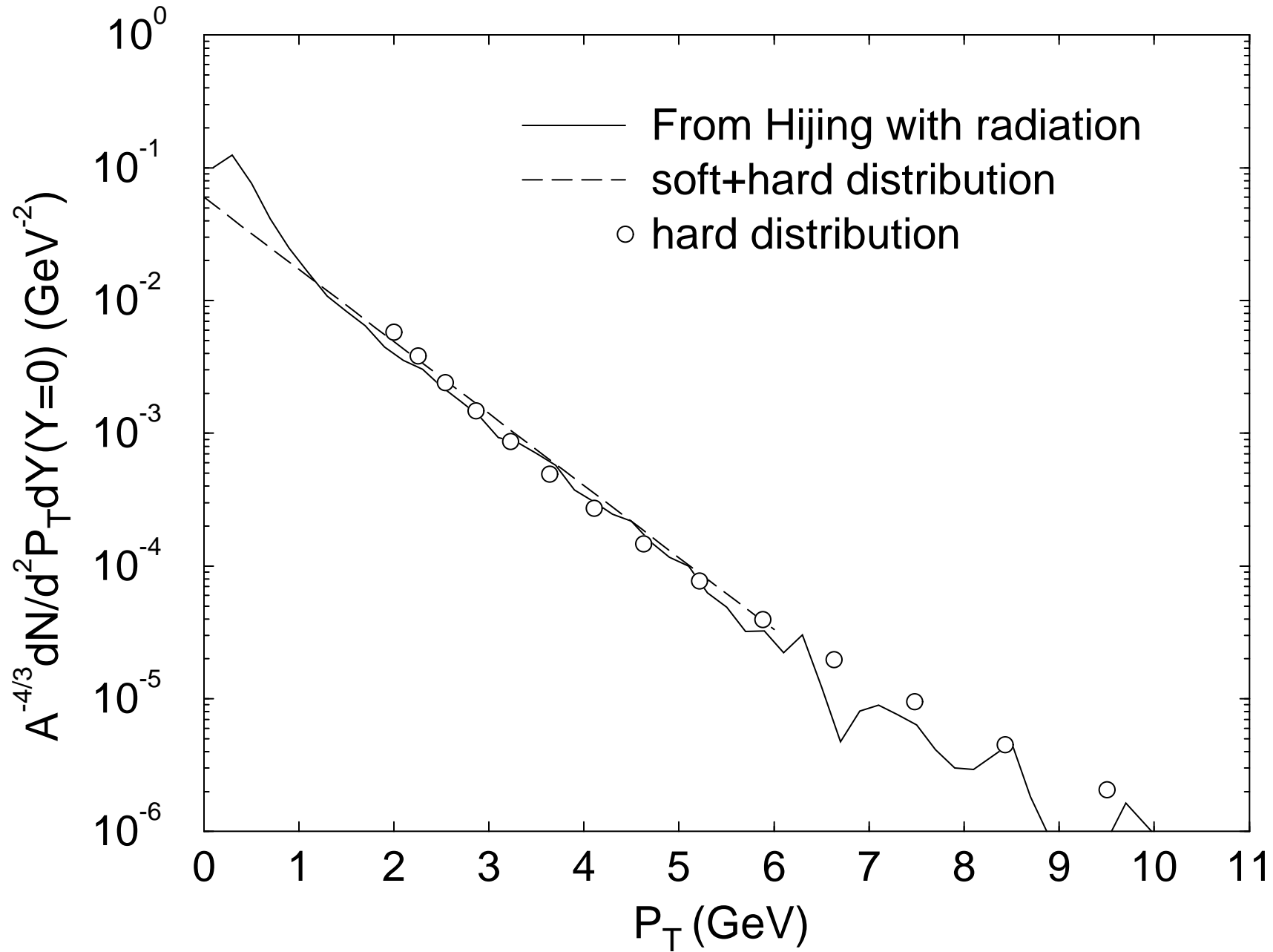


Fig. 6

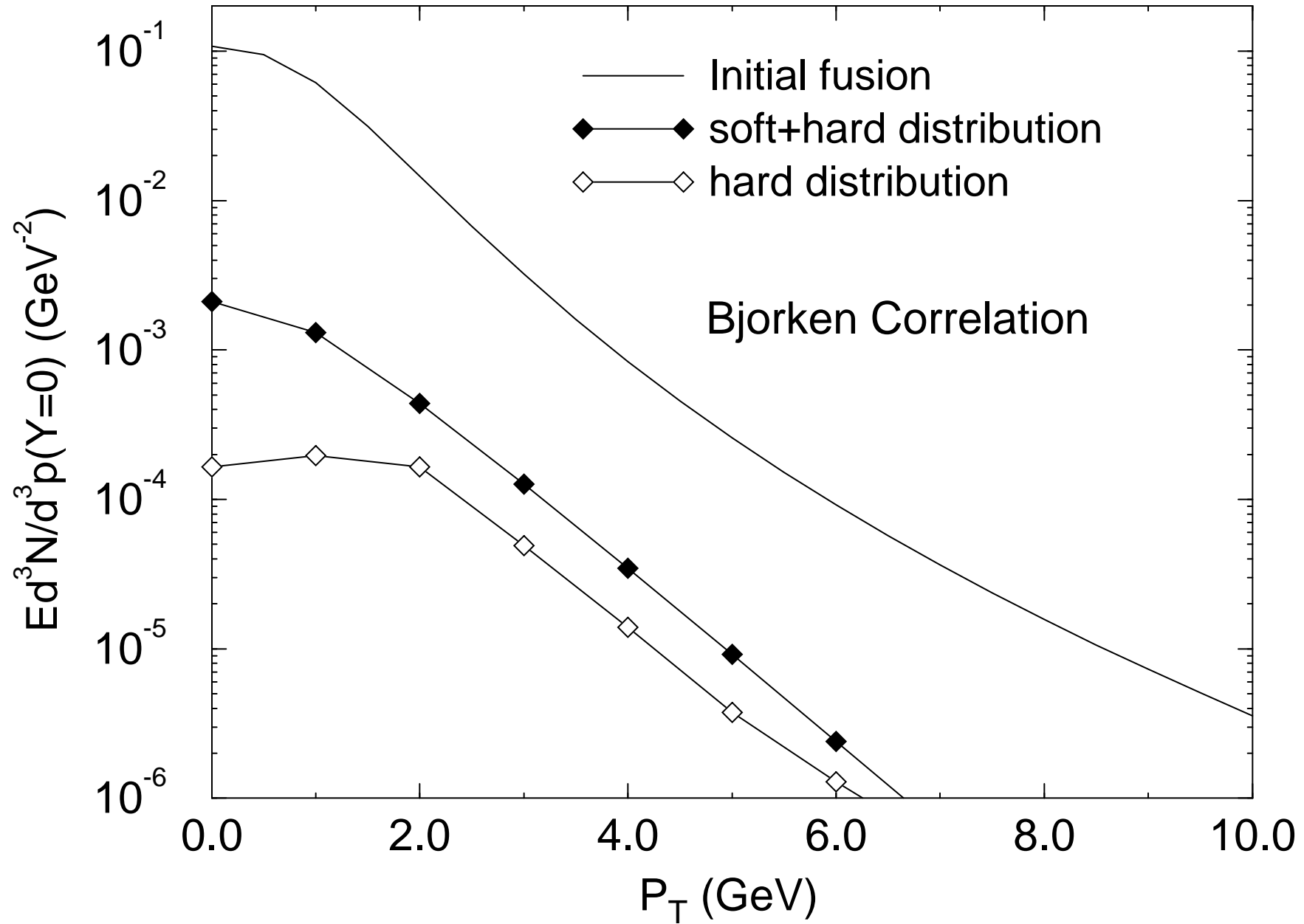


Fig. 7

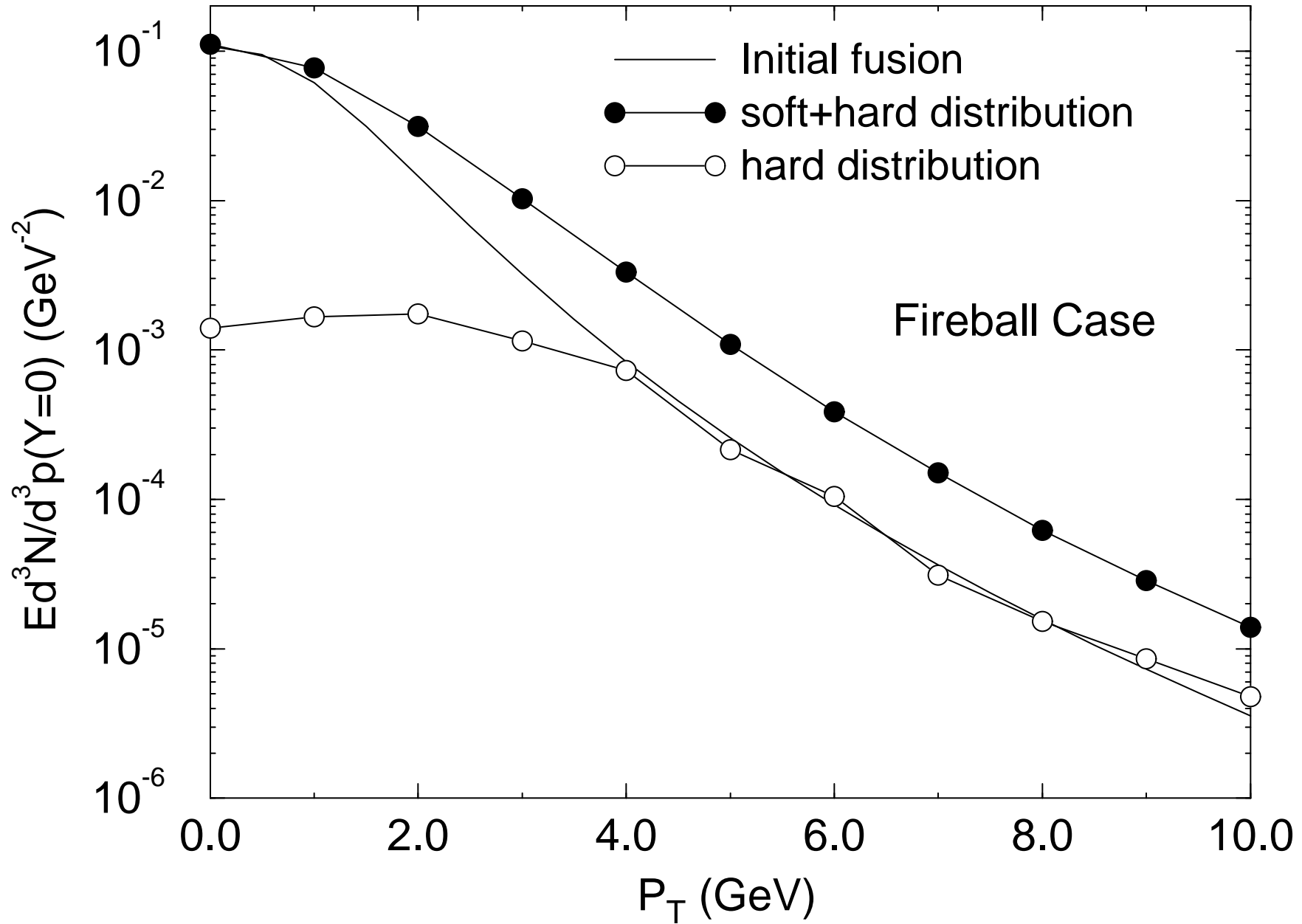


Fig. 8

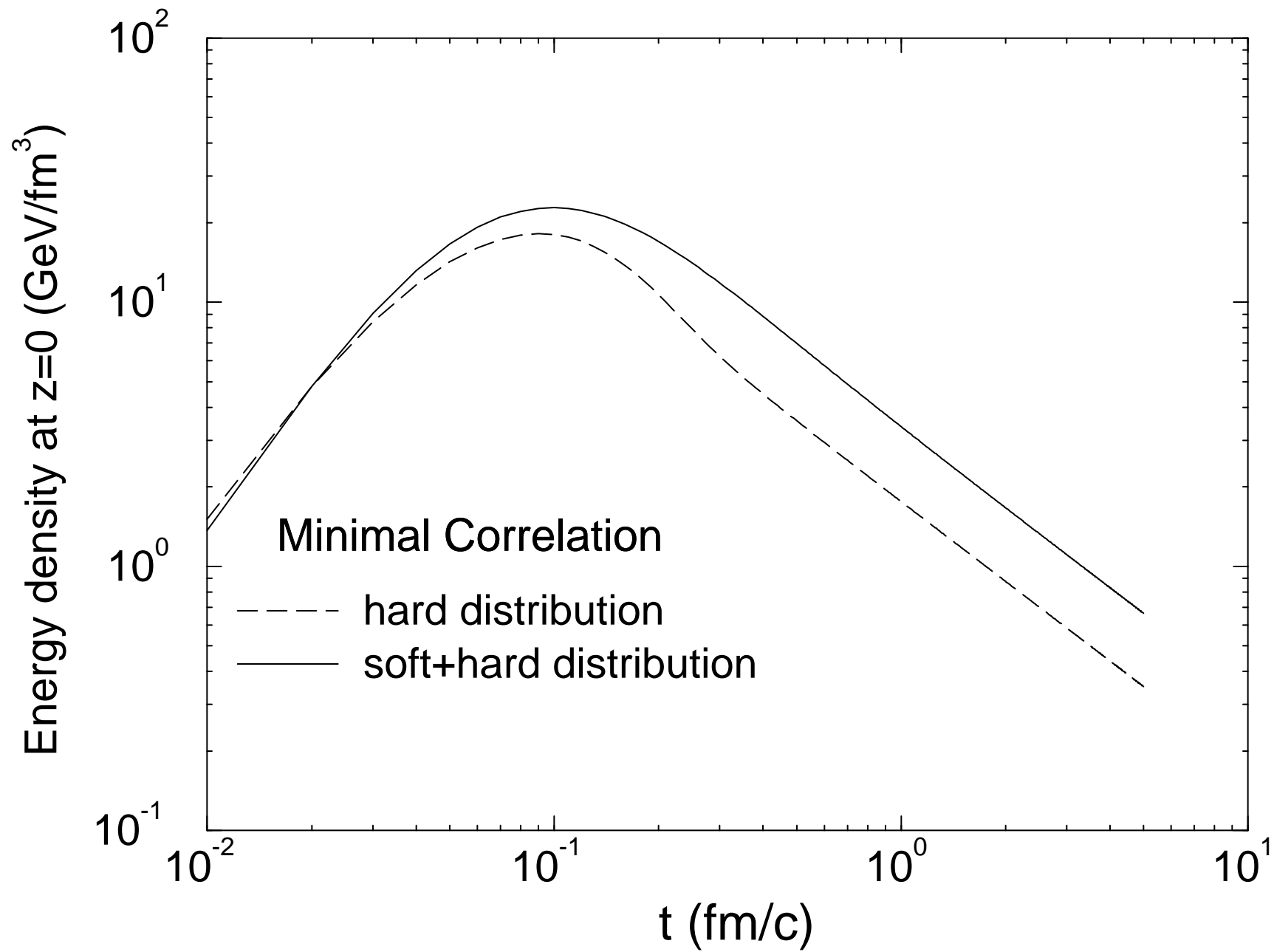


Fig. 9

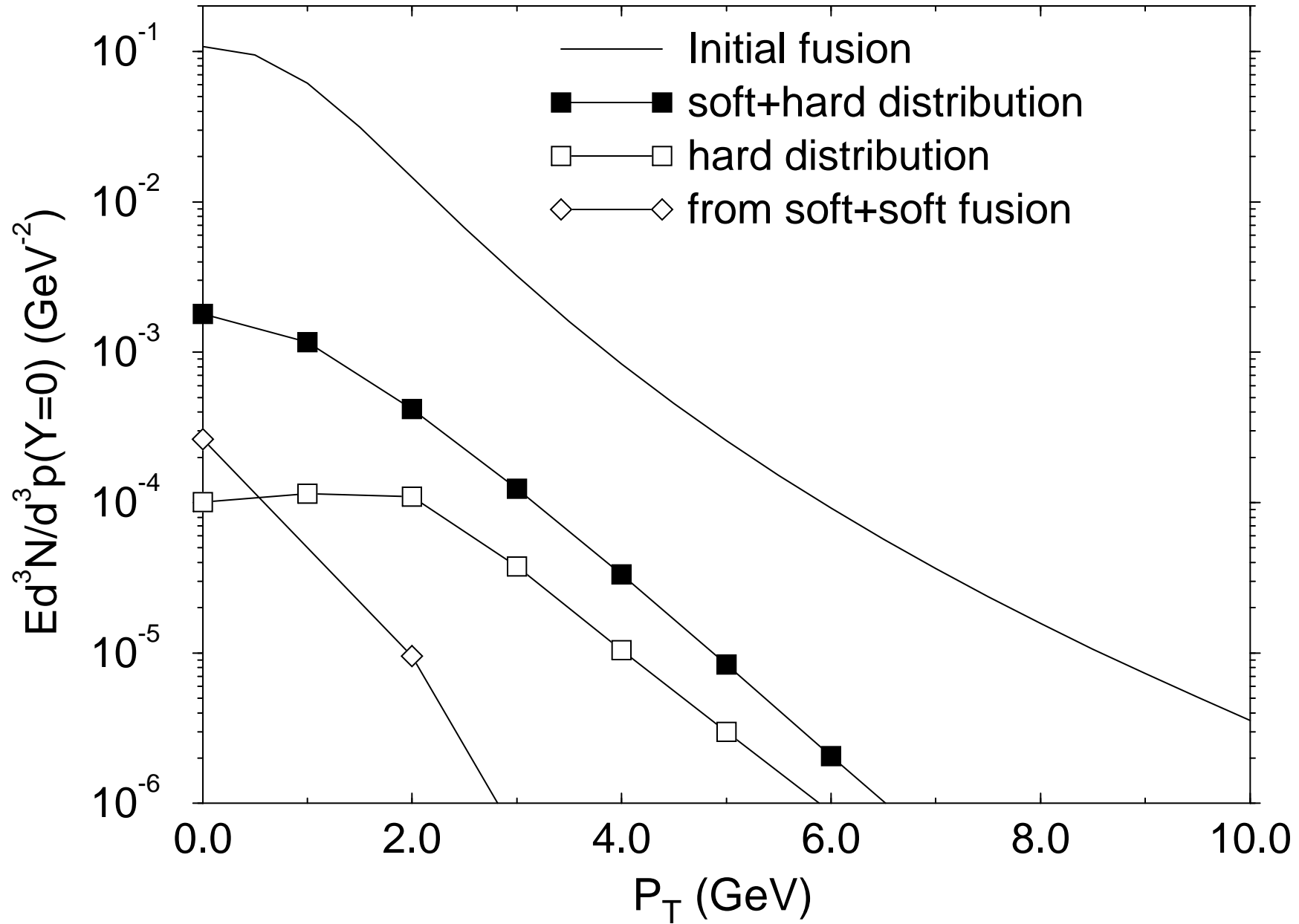


Fig. 10

